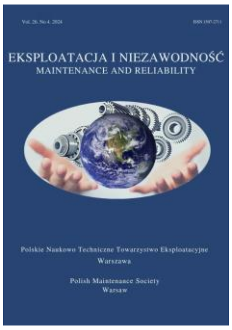

Eksploatacja i Niezawodnosc – Maintenance and Reliability

Volume 26 (2024), Issue 4

journal homepage: http://www.ein.org.pl

Article citation info:
Yun M, Ren J, Zhang L, Chen X, Fracture Process and Instability Precursor Determination of Freeze-thaw Red Sandstone Based on Acoustic Emission Monitoring, Eksploatacja i Niezawodnosc – Maintenance and Reliability 2024: 26(4) http://doi.org/10.17531/ein/191193

Indexed by: Web of Science Group

Fracture Process and Instability Precursor Determination of Freeze-thaw Red Sandstone Based on Acoustic Emission Monitoring

Mengchen Yun[a,*], Jianxi Ren[a], Liang Zhang[a], Xu Chen[b]

[a] School of Architecture and Civil Engineering, Xi'an University of Science and technology, China
[b] School of Civil Engineering, Southwest Jiaotong University, China

Highlights

- Examines the crack initiation strength, damage strength, and peak strength of freeze-thaw red sandstone under different levels of confining pressure.
- The stress-strain curve of sandstone is divided into five stages using the elastic volumetric strain curve and the crack volumetric strain curve.
- Cumulative counting of acoustic emission events can be used to predict the damage of freeze-thaw red sandstone.

Abstract

Research on the damage and fracture mechanism of freeze-thaw (F-T) rocks under loading is a key scientific endeavor derived from numerous safety concerns in cold region rock mass engineering. This study analyzed the relationship between the entire triaxial compression process of the red sandstone and acoustic emission parameters. Based on the nonlinear growth characteristics of cumulative event counts of acoustic emission, a predictive method was proposed for determining the crack initiation strength, damage strength, and failure strength of F-T sandstone. The results demonstrated that this method exhibited good consistency with the crack volume strain approach and accurately and conveniently predicted sample failure strength. The fitted curve of the equation closely aligned with experimental data. These findings offer insights into the classification of damage and fracture mechanisms in F-T sandstone and provide valuable groundwork for research on rock failure prediction and forecasting methods employing acoustic emission monitoring.

Keywords

freeze-thaw sandstone, triaxial compression, rupture process, acoustic emission parameter, precursor information

1. Introduction

Rock engineering construction has experienced rapid growth due to the escalating demands for infrastructure and energy development worldwide. As a result, an increasing number of rock engineering projects are delving into deeper geological strata and high-altitude cold regions, thereby encountering more intricate engineering geological environments [1-3]. Natural rock masses exhibit a plethora of macro and microscopic fractures or defects owing to geological evolution, tectonic movements, weathering, and freeze-thaw (F-T) cycles. The original stress equilibrium of the rock mass is perturbed during rock engineering construction, leading to deformations or cracks, which can culminate in instability and failure of the rock mass. This presents a significant hazard to construction safety and can precipitate rock engineering disasters [4-6].

Currently, research methodologies for investigating rock mechanical properties and failure mechanisms predominantly focus on numerical simulation calculations, physical model experiments, and indoor rock mechanics tests [7-10]. Although

(*) Corresponding author.
E-mail addresses: M. Yun (ORCID: 0000-0003-0600-0258) yunmc1019@163.com, J. Ren (ORCID: 0000-0001-8494-7442) renjianxi1968@163.com, L. Zhang (ORCID: 0000-0003-0228-7159) 963082640@qq.com, X. Chen (ORCID: 0000-0001-5924-0373) xustcx1994@163.com.

numerical simulations calculations can reflect internal fracture mechanisms and stress change patterns in rocks, their effectiveness requires enhancement due to challenges in accurately defining various rock parameters. Moreover, large-scale physical model experiments for simulating rock engineering have limitations due to size effects and physical-mechanical similitude ratios, making it challenging to accurately represent rock parameters and properties. Rock mechanics laboratory tests offer the advantage of comprehensive equipment and monitoring techniques. Utilizing these tests to measure various physical and mechanical indices of rocks is the most effective and reliable approach for analyzing and understanding rock failure mechanisms [11-14]. The process of rock loading leading to failure is accompanied by acoustic emission, reflecting extensive information about internal damage processes in rocks, including internal deformation, initiation and propagation of new cracks, and energy release in the form of elastic waves during rock fracture and failure [7]. Due to the ongoing development and refinement of acoustic emission technology, numerous scholars have investigated the correlation between distinct acoustic emission parameters and rock stress-strain behavior, along with failure characteristics [15-21]. Nevertheless, current research primarily utilizes acoustic emission technology to aid in monitoring rock instability and failure processes. However, there remains an incomplete understanding of crack initiation, propagation, and coalescence in rocks subjected to coupled effects of F-T and loading, as well as a need for a comprehensive method to precisely predict and forecast initiation stress, damage stress, and peak stress.

This study utilized red sandstone subjected to F-T cycles as the experimental material. Triaxial compression tests were performed under varying confining pressures, and acoustic emission parameters were simultaneously collected. By incorporating the theory of crack volume strain [22-25] and considering the features of acoustic emission parameters, the initiation strength and damage strength characteristics of F-T sandstone under triaxial stress were investigated. Furthermore, based on the cumulative event parameters of acoustic emission, a damage evolution equation for F-T sandstone under triaxial compression conditions was formulated. These research findings contribute to a deeper comprehension of fracture and disaster incubation mechanisms in cold regions rocks, establish a rock fracture prediction approach relying on acoustic emission, and offer insights for assessing and forecasting rock mass engineering failures and significant geological disasters in cold regions.

2. Material and methods

2.1. Sample preparation and experimental equipment

(1) Sample preparation

The collected red sandstone is processed into standard cylindrical samples with a diameter of 50 mm and a height of 100 mm in the laboratory. Subsequently, ultrasonic inspection is conducted to ensure the selected samples exhibit good consistency. (Fig. 1). The basic physical parameters of the samples were measured and presented in Table 1. It is observed that the selected samples exhibited a density range of 2.04 to 2.14 g/cm³, with an average value of 2.09 g/cm³. The Compression wave velocity varied from 2.08 to 2.20 km/s, with an average value of 2.15 km/s.

Fig. 1. Sandstone samples.

Table 1. Details of sandstone samples.

Sample number	Volume [cm³]	Dry mass [g]	Saturated mass [g]	Dry density [g/cm³]	Porosity [%]	Saturation coefficient	Compression wave velocity [km/s]
W-1	189.46	402.89	434.64	2.12	16.76	0.82	2.17
W-2	186.92	400.11	430.01	2.14	16.00	0.76	2.14
W-3	187.68	393.70	427.43	2.09	17.97	0.76	2.11
W-4	189.63	386.85	418.27	2.04	16.57	0.80	2.19
W-5	191.30	401.24	431.53	2.10	15.83	0.84	2.20
W-6	190.45	388.52	421.98	2.04	17.57	0.91	2.08

(2) Experimental equipment

The experiment utilized the GCTS servo-controlled rock triaxial testing system (Fig. 2), which was equipped with an acoustic emission monitoring system. It provided two loading methods: strain-controlled and stress-controlled. The maximum axial load was 1500 kN, and the maximum confining pressure was 140 MPa, both with an accuracy of 0.1%. The triaxial compression chamber was equipped with the PAC-DISP series, featuring an 8-channel fully digital acoustic emission monitoring system. This setup facilitated the placement of four to eight acoustic emission sensors on the sample surface, enabling integration of acoustic wave and acoustic emission monitoring. The system exhibited excellent data acquisition and three-dimensional localization capabilities. In this study, six acoustic emission probes were positioned: three at each of the upper and lower ends, arranged in a triangular pattern, with each probe situated 25mm away from the top and bottom ends of the sample (Fig. 2c).

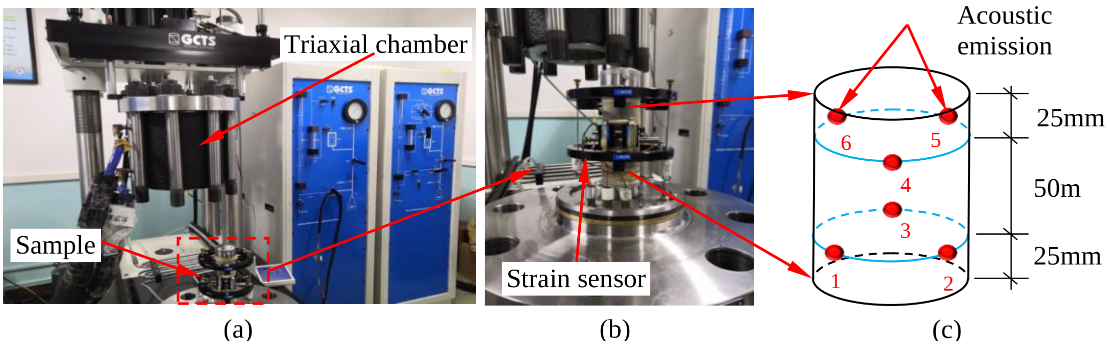

Fig. 2. Experimental equipment: (a) GCTS testing system, (b) sample mounting, and (c) position of acoustic emission probes.

2.2. Experimental scheme

(1) Freeze-thaw test

Initially, the sandstone was inserted into a forced saturator for vacuum pumping and water saturation treatment. Subsequently, the saturated sample was placed into the freeze-thaw environment box for water replenishment freeze-thaw cycle once, with a freezing temperature of -20 ℃. After freezing for 48 h, the sample was thawed at 20 ℃ for 48 h (Fig. 3a). The temperature change rate in the freeze-thaw cycle was 60 ℃/h. The freeze-thaw cycle test chamber has an automatic control function, the temperature variation range is -50~50 ℃, the accuracy is 0.1 ℃, and it can work continuously for more than 60 d.

(2) Triaxial compression tests

Triaxial compression tests were performed at three distinct confining pressure levels (2 MPa, 4 MPa, and 6 MPa). Initially, axial and confining pressures were incrementally applied to predetermined values at a constant rate using stress-controlled loading under static water pressure conditions, with a loading rate of 1 MPa/min. Subsequently, upon reaching static water pressure equilibrium, axial pressure was incrementally applied using strain-controlled loading until failure occurred, with a loading rate of 0.1 mm/min (Fig. 3b).

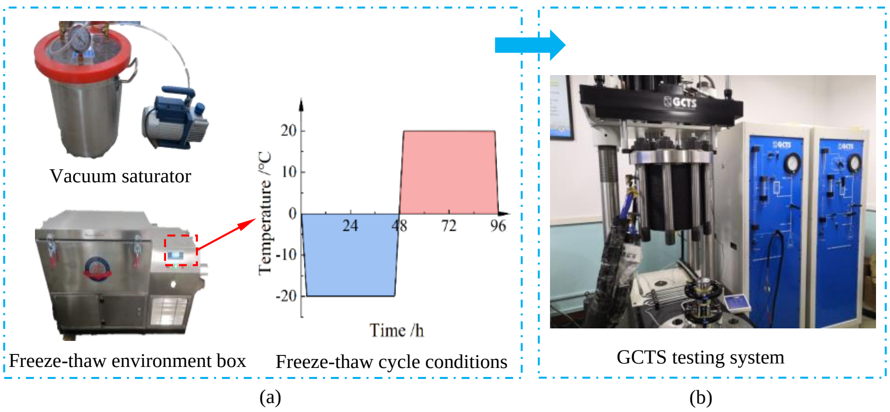

Fig. 3. Experimental flowchart: (a) freeze-thaw test and (b) triaxial compression tests.

3. Results and discussion

3.1. Characteristics of sandstone after freeze-thaw cycle

The red sandstone undergoes drying after the freeze-thaw cycle, and the loss rate can be calculated based on the mass after drying and the compression wave velocity, as illustrated in Fig. 4. The mass and compression wave velocities of red sandstone exhibit losses after freeze-thaw cycle. The mass loss is minimal, with the loss rate primarily falling within the range of 0.29% to 0.40%. However, the loss in wave velocity is more significant, with the highest loss rate reaching 34%. Additionally, The SEM results indicate the deterioration of the sandstone microstructure before and after freeze-thaw cycle (Fig. 5). In its natural state, the surface of sandstone crystals is smooth and intact. However, after freeze-thaw cycle, it becomes rough, and new cracks appear on the crystals. This indicates that frost heave forces weaken grain cementation, causing grain detachment and internal pore formation in sandstone, ultimately leading to a decrease in macro-scale compression wave velocity.

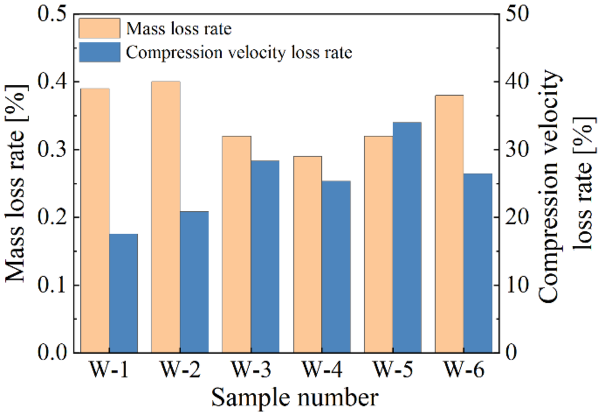

Fig. 4. Loss rate of red sandstone after freeze-thaw cycle.

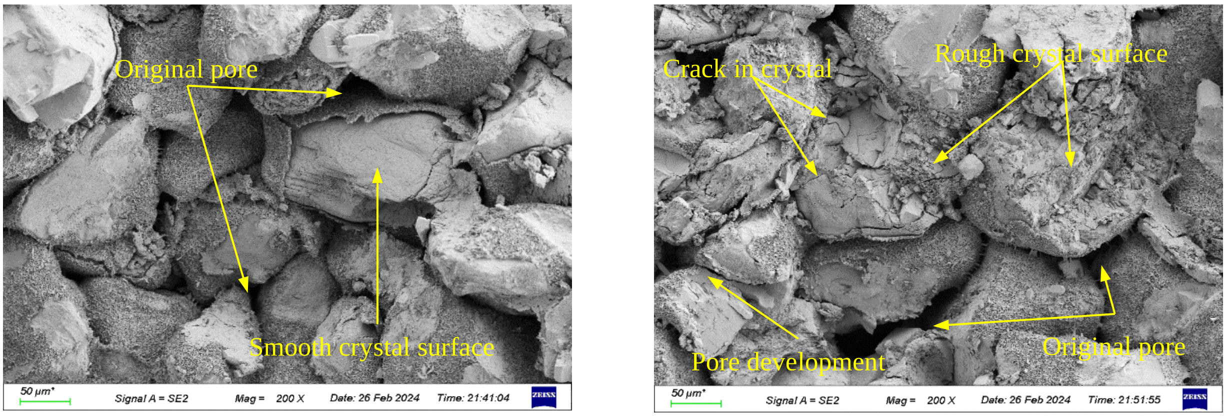

Fig. 5. The SEM images of red sandstone under different conditions: (a) natural conditions and (b) After freeze-thaw cycle.

3.2. Mechanical properties analysis

The triaxial compression stress-strain curves for red sandstone under different confining pressure levels were shown in Fig. 6. The curves revealed that with the increasing confining pressure, both the compressive strength and peak strain of the sample gradually increase. Similarly, the compressive strength and strain at the dilatancy point also exhibit a gradual increase. As the confining pressure increased from 2 MPa to 6 MPa, the ratios of dilatant stress to peak strength were 74.29%, 63.82%, and 85.51%, respectively, yielding an average value of 74.54%. This indicates a moderate volumetric dilatancy rate. The average modulus and secant modulus effectively characterize the deformation properties of the rock. Table 2 presents the peak strength and deformation parameters of the samples at various confining pressure levels. At lower confining pressure levels, the samples displayed lower peak strength and noticeable softening. As the confining pressure increased, both the peak strength and peak strain of the samples gradually increased. Additionally, both the average modulus and secant modulus increased, while the Poisson's ratio exhibited a decreasing trend.

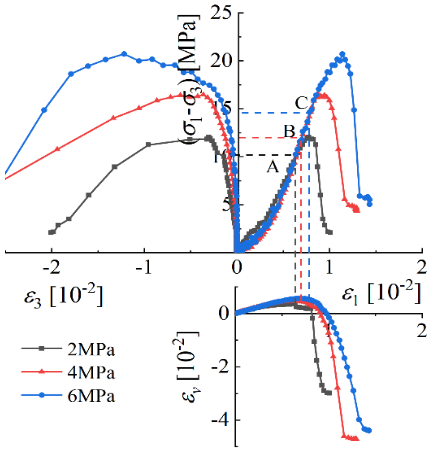

Fig. 6. Stress-strain curves of sandstone under different confining pressures.

Table 2. Strength and deformation parameters of the sandstone samples.

Confining pressure(MPa)	Peak strength[MPa]	Peak strain[%]	Average modulus[GPa]	Secant modulus[GPa]	Poisson ratio
2	15.91	1.107	21.074	12.264	0.27
4	20.87	1.158	26.931	17.136	0.25
6	23.88	1.201	28.392	18.714	0.23

The crack volumetric strain could effectively reflect the rock's crack closure stage and crack initiation stag. The initiation strength represents the starting point of stable crack extension, while the damage strength represents the starting point of unstable crack extension. The study of rock crack initiation strength and damage strength is significant importance. It can be calculations as follows:

$$\varepsilon_V^c = \varepsilon_V - \frac{1-2\mu}{E}[(\sigma_1 + \sigma_2 + \sigma_3)] \tag{1}$$

In the equation: ε_V^c represented the crack volumetric strain of the sandstone; ε_V represented the elastic volumetric strain of the sandstone; σ_1、σ_2 and σ_3 were the principal stresses in the three loading directions; E and μ represented the elastic modulus and Poisson's ratio of the sandstone, respectively.

Using the axial stress, axial, and circumferential strains acquired from the triaxial compression tests, the elastic volumetric strain and crack volumetric strain curves of sandstone samples under various confining pressure levels can be calculated using the Equation (1), as shown in Fig. 7. The curves illustrate that the stress-strain curves of F-T sandstone under triaxial compression conditions can be divided into five stages using the elastic volumetric strain and crack volumetric strain curves: the pore compaction stage (segment *o-a*), the linear elastic deformation stage (segment *a-b*), the stable crack extension elasto-plastic deformation stage (segment *b-c*), the unstable crack extension plastic deformation stage (segment *c-d*), and the post-peak failure stage (segment *d-e*).

The crack initiation strength σ_{ci} and the damage strength σ_{cd} of F-T sandstone under various confining pressures could be directly determined by strength values corresponding to points *b* and *c* in the Fig. 6 and Table 3. The increase in confining pressure was observed to inhibit the failure of F-T sandstone and enhanced the ductility of the rock samples under certain conditions. This was evidenced by the increase in both the initiation strength and peak strength of F-T sandstone with increasing confining pressure, accompanied by a decrease in the corresponding initiation strain and peak strain. At various confining pressure levels, the ratios of initiation strength to peak strength were 0.41, 0.35, and 0.43, respectively, with corresponding strain ratios of 0.60, 0.52, and 0.53. The initiation strength of the F-T sandstone ranged from approximately 0.3 to 0.5 times the peak strength. The ratios of damage strength to peak strength were 0.79, 0.69, and 0.71, respectively, with corresponding strain ratios of 0.78, 0.71, and 0.69. This indicates that the damage is approximately 0.7 to 0.8 times the peak strength. Therefore, the crack volumetric strain may be utilized to accurately estimate the initiation and damage stages of the F-T sandstone.

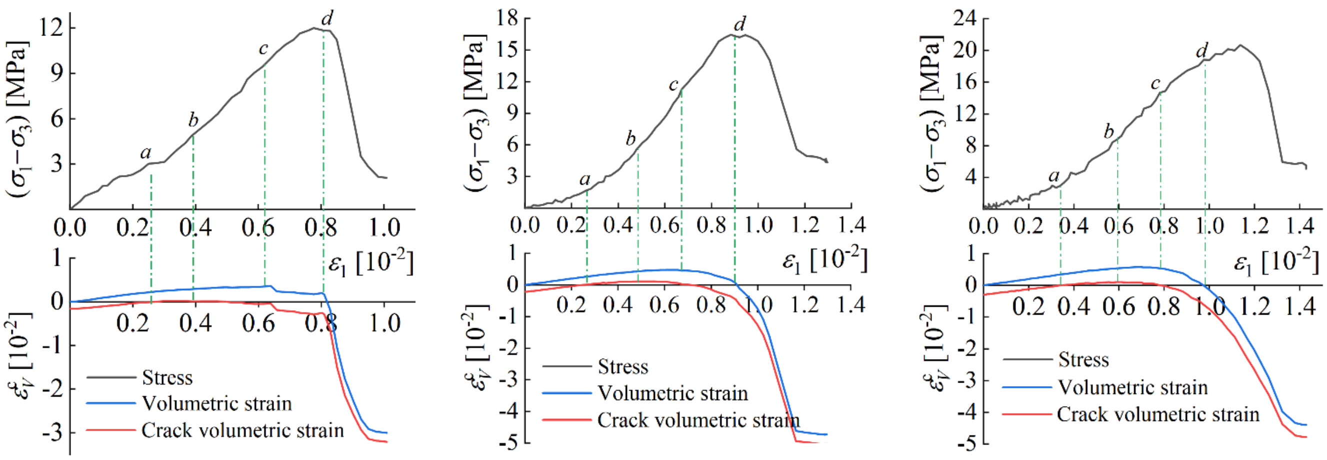

Fig. 7. Variation of sandstone volume strain and crack volume strain curves under different confining pressure: (a) confining pressure of 2 MPa, (b) confining pressure of 4 MPa, and (c) confining pressure of 6 MPa.

Table 3. Strength and deformation parameters of the Samples.

Confining pressure [MPa]	σ_{c_c}[MPa]	$\frac{\sigma_{c_c}}{\sigma_f}$	σ_{c_i}[MPa]	$\frac{\sigma_{c_i}}{\sigma_f}$	σ_{cd}[MPa]	$\frac{\sigma_{c_d}}{\sigma_f}$	σ_f[MPa]
2	3.07	0.25	4.96	0.41	9.63	0.79	12.1
4	1.68	0.11	5.75	0.35	11.33	0.69	16.4
6	3.04	0.15	8.90	0.43	14.7	0.71	20.7
Confining pressure [MPa]	ε_{c_c}[%]	$\frac{\varepsilon_{c_c}}{\varepsilon_f}$	ε_{c_i}[%]	$\frac{\varepsilon_{c_i}}{\varepsilon_f}$	ε_{cd}[%]	$\frac{\varepsilon_{c_d}}{\varepsilon_f}$	ε_f[%]
2	0.26	0.33	0.39	0.50	0.62	0.79	0.78
4	0.26	0.27	0.49	0.52	0.67	0.71	0.95
6	0.34	0.30	0.60	0.53	0.79	0.69	1.14

3.2. Analysis of crack strain and acoustic emission event count characteristics

Sandstone experienced a localized material change during the loading process, resulting in an acoustic emission event. A triaxial compression test was conducted on the sandstone, complemented by acoustic emission detection methods. Parameters including the count rate, energy rate, and cumulative energy of acoustic emissions were recorded throughout the experiment. The correlation between crack volume strain and acoustic emission parameters was investigated, with the experimental findings presented in Fig. 8.

Fig. 8a illustrates the distribution curves of volume strain and crack volume strain against axial strain. By analyzing the volume strain and crack volume strain curves, the stress-strain curve of F-T sandstone under triaxial compression conditions could be distinctly segmented into five stages: pore compaction, linear elastic deformation, stable crack expansion elastoplastic deformation, unstable crack expansion plastic deformation, and post-peak failure phases.

Fig. 8b illustrates the distribution curves of the stress-strain curve, acoustic emission energy rate, and count rate. Prior to reaching their peak strength, the acoustic emission energy rate curve of the F-T sandstone specimens remained nearly constant, exhibiting no significant abrupt changes. A significant sudden increase in the energy rate occurred only upon reaching peak strength, with the rate momentarily spiking to an extreme value before rapidly returning to zero. During the development of the stress, the event count rate of acoustic emission distribution exhibited two points with notably accelerated growth, identified as points *P* and *Q*. Preceding point *P*, the event rate remained consistently low. Subsequent passing point *P*, a distinct upward trend ensued, persisting until just prior to the inflection point *Q*, where a brief decline was observed. Upon reaching point *Q*, the event rate surged, continuing until a sudden drop occurred near the peak strength, leading to the instability and failure of the specimen. The stress intensity value at point *P* was 9.17 MPa, and at point *Q* was 11.86 MPa, corresponding to 0.76 and 0.98 times the peak strength, respectively. This was consistent with the damage strength of the sandstone as listed in Table 3.

Fig. 8c displayed the distribution curves depicting the stress-strain relationship, cumulative count, and the rate of change in cumulative count. The cumulative count rate of change curve exhibited three distinct inflection points, labeled, *M*, *N*, and *R*, effectively segmenting it into four stages. Before point *M* (Stage I), the rate of cumulative count increase remained nearly zero, gradually escalating thereafter until point *N* (Stage II) where it declined. Subsequently, it steadily rose until reaching a peak at point *R* (Stage III), sharply declining thereafter to zero beyond point *R* (Stage IV). Concurrently, the stress values at points *M*, *N*, and *R* on the cumulative count rate of change curve were 3.58 MPa, 8.61 MPa, and 11.86 MPa, respectively, accounting for 30%, 71%, and 98% of the peak strength. Thus, a combined analysis of the count rate and cumulative count curves facilitates the determination of both the initiation strength and damage strength of F-T sandstone, along with a dependable forecast of its peak strength upon failure.

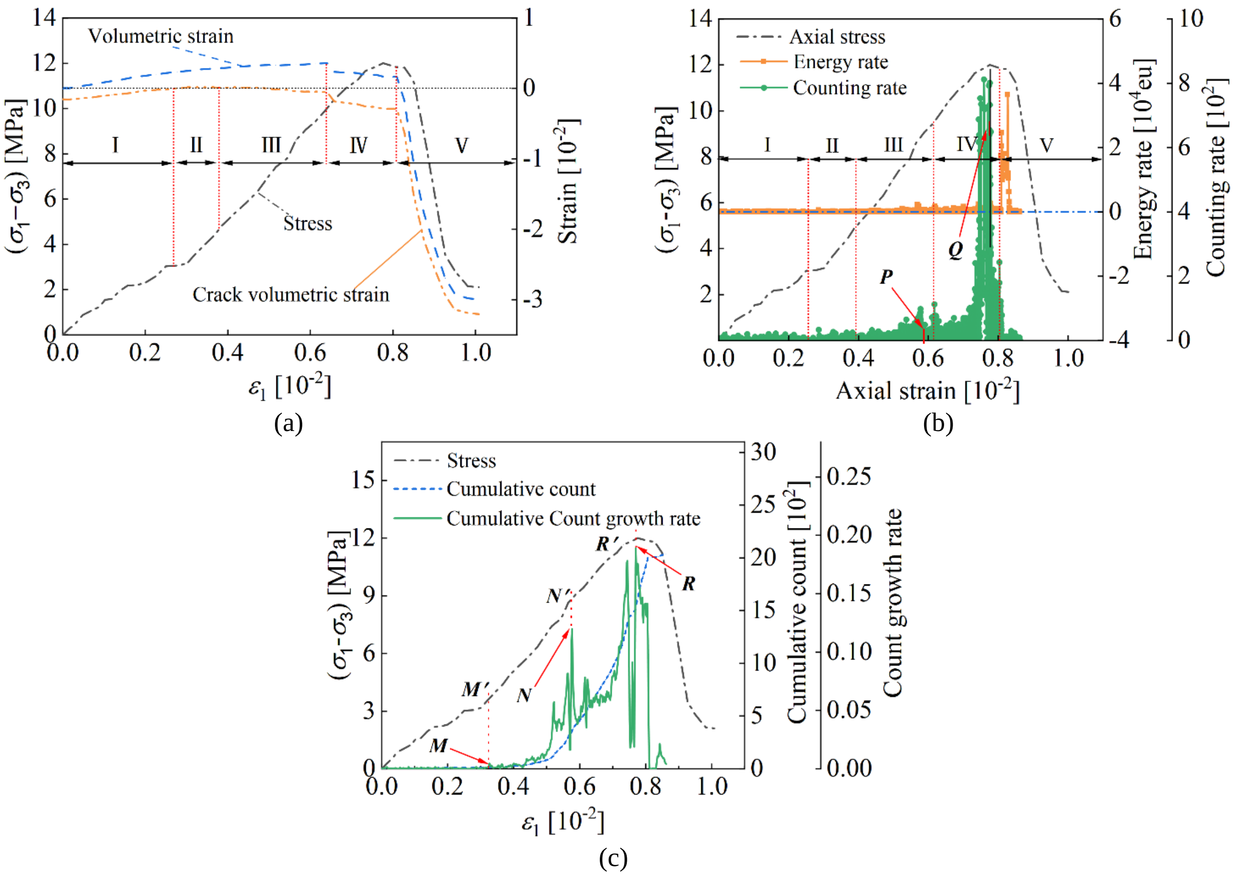

Fig. 8. Stress-strain and acoustic emission parameters variation curve: (a) stress-strain curve, variation diagram of volume strain and crack volume strain, (b) stress-strain curve, corresponding energy rate and counting rate variation diagram, and (c) stress-strain curve, corresponding cumulative counting rate and cumulative technical growth rate variation diagram.

The stress which the first deviation from the linear portion of the cumulative count curve was identified as the crack initiation stress. Upon reaching the damage strength, the cumulative count curve of the sandstone sample displayed an immediate upward trend. The stress at which the extended line of the second deviation portion of the event curve intersected with the first deviation from the linear portion was identified as the damage stress. Based on these criteria, Fig. 9 illustrates the relationship between crack initiation stress, damage stress, and cumulative event. The analysis indicated that the crack initiation strength $\sigma_{ci}{}'$ and damage strength $\sigma_{cd}{}'$ of the sandstone samples under various confining pressures, determined by the inflection points of the cumulative count curve, correlated well with the strength values derived from the crack volume strain. Specific parameters were shown in Table 4.

It could be summarized as follows: Under triaxial compression conditions, when the stress applied to the sandstone sample was less than the crack initiation stress $\sigma_{ci}{}'$, the internal pores and fractures were compacted without the generation of new cracks, resulting in a low level of acoustic emission cumulative count. When the applied deviatoric stress exceeded the crack initiation stress $\sigma_{ci}{}'$ but remained below the damage stress, the sandstone sample initiated microcrack development, leading to a gradual increase in the acoustic emission cumulative count, indicative of stable crack propagation. Once the applied deviatoric stress exceeded the damage stress $\sigma_{cd}{}'$, the cumulative count of acoustic emissions surged, signifying that the sandstone sample entered the stage of unstable crack propagation and coalescence. Subsequently, when the applied deviatoric stress exceeded the peak stress σ_R, the acoustic emission cumulative count increased linearly. With the internal cracks fully developed, the sandstone structure failed. The Figure indicated that the damage stress values under different confining pressures were fully approximately 11.86 MPa, 15.91 MPa, and 19.99 MPa, corresponding to approximately 98%, 97%, and 97% of the peak strength, respectively. This indicated that the stress σ_R based counting effectively predicts the failure of F-T sandstone under triaxial compression.

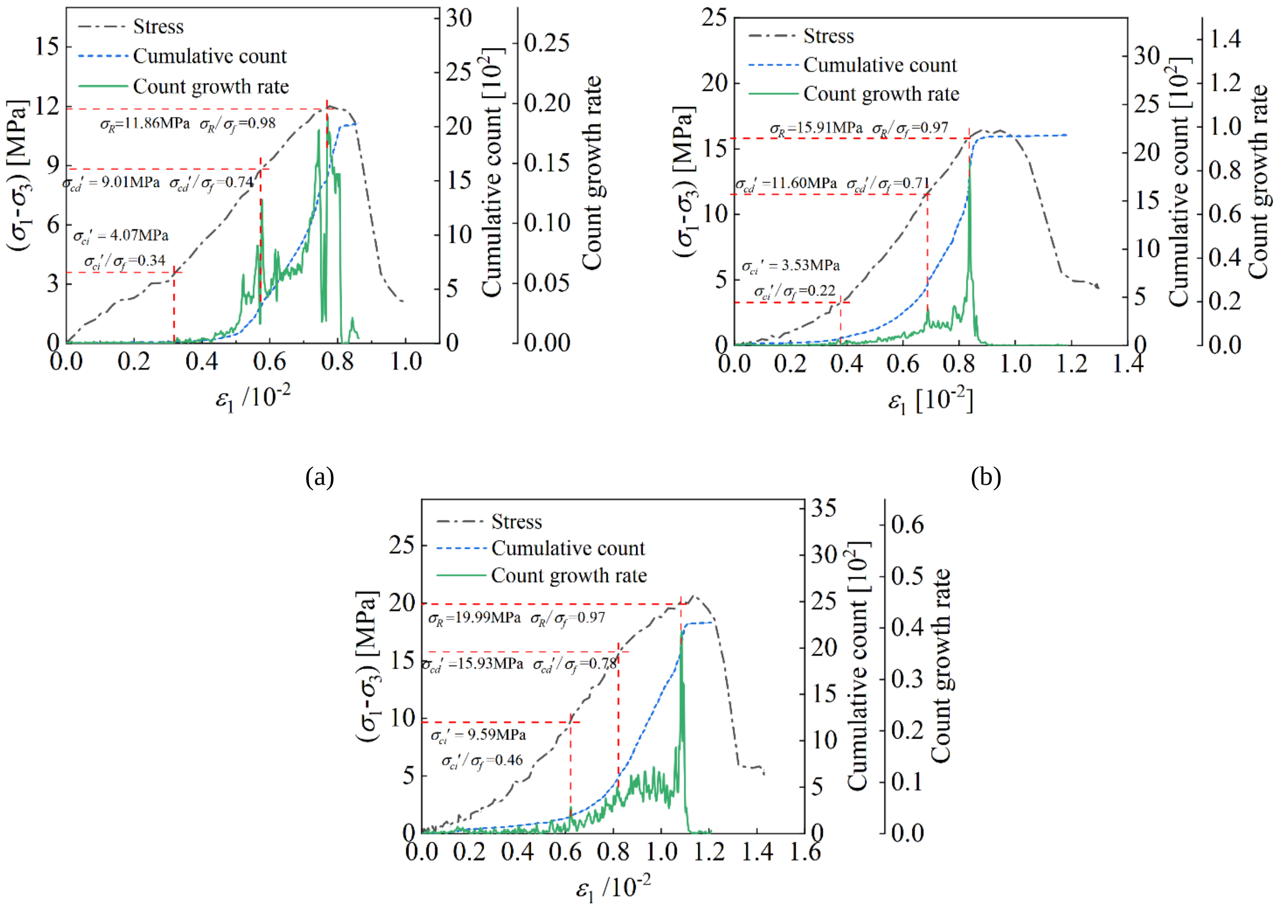

(a) (b)

(c)

Fig. 9. Cumulative count and stress-strain relationship curve: (a) confining pressure of 2 MPa, (b) confining pressure of 4 MPa, and (c) confining pressure of 6 MPa.

Table 4. Stress parameters of sandstone under different confining pressures.

Confining pressure [MPa]	σ_{ci}' [MPa]	$\frac{\sigma_{ci}'}{\sigma_f}$	σ_{cd}' [MPa]	$\frac{\sigma_{cd}'}{\sigma_f}$	σ_R [MPa]	$\frac{\sigma_R}{\sigma_f}$	σ_f [MPa]
2	5.42	0.45	9.01	0.74	11.86	0.98	12.1
4	3.53	0.22	11.6	0.71	15.91	0.97	16.4
6	9.59	0.46	19.99	0.78	19.99	0.97	20.7

4. Establishment of damage evolution equation

Acoustic emission parameters are closely associated with rock damage and failure. The occurrence of new cracks within rocks, the failure of pre-existing fissures, and the eventual unstable failure process are all accompanied by acoustic emission phenomena. These emissions serve as indicators of the damage evolution pattern in rocks, facilitating the formulation of a damage evolution equation. Thus, to precisely depict the damage evolution pattern of F-T sandstone, the cumulative count of acoustic emission events was employed as a variable to quantify the damage in F-T sandstone, assuming damage equivalence.

The damage variable was defined as:

$$D = \frac{A_d}{A} \tag{2}$$

In the formula: D represents the damage variable, A represents the effective cross-sectional area of the sandstone in its initial state, and A_d represents the effective area of the sandstone at the point of damage occurrence.

Thus, the cumulative count of acoustic emission events per unit area of sandstone when damaged is:

$$V_t = \frac{V_s}{A} \tag{3}$$

In the formula: V_t represents the cumulative count of acoustic emission events per unit area when the sandstone is damaged, and V_s represents the cumulative count of acoustic emission events when the sandstone experiences complete destruction.

Therefore, when the cumulative count of acoustic emission events for sandstone reaches V_d, it can be expressed as:

$$V_d = A_d \frac{V_s}{A} \tag{4}$$

By combining equations (3) and (4), we can derive the relationship between the damage variable D of sandstone and the cumulative count of acoustic emission events as follows:

$$D = \frac{V_d}{V_s} \tag{5}$$

Establishing the probability density function $F(\sigma)$ based on the axial strain and cumulative count of acoustic emission events generated by F-T sandstone under load involves:

$$F(\varepsilon)d(\varepsilon) = dV_d/V_d \tag{6}$$

$$F(\varepsilon) = \alpha/\varepsilon + \beta \tag{7}$$

In the formula: α and β represent mechanical properties and internal damage parameters of sandstone, where the magnitude of α indicates the extent of internal damage within the sandstone.

By combining equations (6) and (7), it can be obtained that:

$$V_d = C\varepsilon^{\alpha} \exp(\beta\varepsilon) \tag{8}$$

Finally, combining equations (5) and (8), it can be obtained that:

$$D = \frac{C\varepsilon^{\alpha} \exp(\beta\varepsilon)}{V_s} \tag{9}$$

In the formula: C represents a constant.

Equation (9) was used to fit the cumulative count of acoustic emission events from F-T sandstone specimens under various confining pressure levels during triaxial compression, and the results are presented in Fig. 10. It is noticeable that at various confining pressure levels, the cumulative count increases gradually in the initial stages of the test. However, upon reaching the rock's cracking strength, the cumulative count begins to rise rapidly, peaking at the point of sample failure. This suggests that defining the damage variable based on the cumulative count of acoustic emissions was reasonable and practical. Additionally, by substituting the experimental results into equation (9), the damage parameters α and β can be determined, as presented in Table 5. It was evident that with increasing confining pressure, the values of parameter α decreased from 9.84 to 5.77. This implies that the effect of confining pressure led to compaction of internal pores and closure of some original cracks within the sandstone specimen, resulting in enhanced strength and a more compact internal structure, hence the smaller values of α. Therefore, it can be inferred that the degree of damage in F-T sandstone can be assessed based on the magnitude of α.

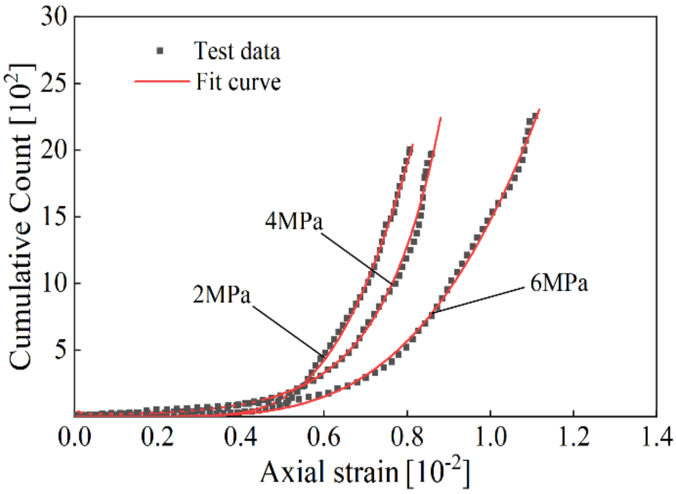

Fig. 10. Fitting curve of cumulative counting of acoustic emissions from F-T sandstone.

Table 5. Damage parameters of F-T sandstone

Confining pressure [MPa]	α	β	R^2
2	9.84	0.079	0.998
4	7.58	0.014	0.994
6	5.77	0.028	0.997

Based on the experimental results, the damage evolution curve of F-T sandstone is presented in Fig. 11. It is apparent that under various confining pressure levels, the damage variable of F-T sandstone exhibits minimal change before the onset of cracking. Following this, the damage variable began to increase, signifying the onset of stable damage development in the sandstone. It is noteworthy that at a confining pressure of 2 MPa, the sandstone initially entered the stage of stable damage development, followed by 4 MPa and then 6 MPa. With increasing confining pressure increases, F-T sandstone demonstrates an ability to withstand stronger loads and exhibit greater deformation, indicating that the application of confining pressure enhance its ductility and delays sandstone failure.

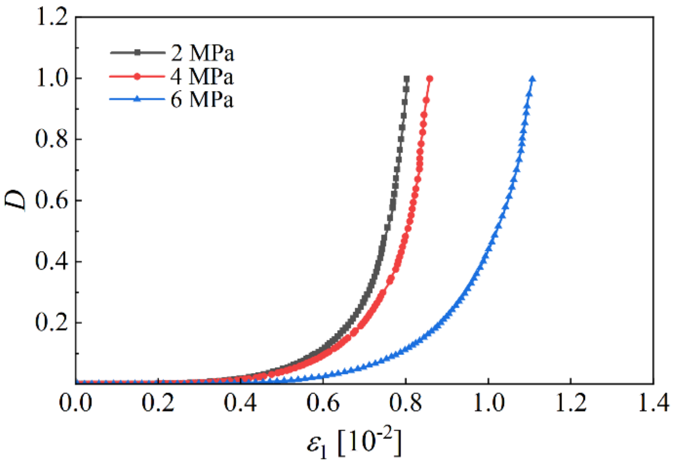

Fig. 11. Damage evolution curve of F-T sandstone under different confining pressure.

5. Conclusion

By conducting triaxial compression acoustic emission tests, the mechanical properties and acoustic emission characteristics of freeze-thaw (F-T) red sandstone under various confining pressures were analyzed and studied. The following main conclusions were drawn:

(1) The full stress-strain curve development of F-T sandstone under various confining pressures exhibited fundamental similarity, characterized by five distinct stages: pore compaction, linear elastic deformation, stable crack expansion elastoplastic deformation, unstable crack expansion plastic deformation, and post-peak failure stages.

(2) The crack volume strain serves as a convenient and accurate indicator of the crack initiation strength and damage strength of F-T sandstone. The crack initiation strength typically ranges from approximately 0.3 to 0.5 times the peak strength, while the damage strength is typically around 0.7 to 0.8 times the peak strength.

(3) The cumulative count curve of acoustic emission events exhibited three distinct inflection points, denoted as M, N, and R, which effectively estimated the initiation strength and damage strength of F-T red sandstone samples. The strength value corresponding to point R was approximately 97% of the peak strength of the sandstone. The characteristics of this point could serve as a precursor to F-T sandstone failure under triaxial compression conditions, offering insights for predicting rock failure using acoustic emission technology.

(4) The cumulative count of acoustic emission events is closely linked to the damage condition of F-T sandstone. Developing a damage evolution equation based on cumulative count is consistent with experimental data and may accurately reflect the law of damage evolution.

Acknowledgements

This study was completed in the college of architecture and civil engineering, Xi'an University of science and technology. This study was supported by the National Natural Science Foundation of China (No. 12072259 and No. 42377187), China Postdoctoral Science Foundation (No. 2022MD723831) and Shaanxi Provincial Natural Science Basic Research Program (No. 2024JC-YBQN-0029).

References

1. Sakurai S. Modeling strategy for jointed rock masses reinforced by rock bolts in tunneling practice. Acta Geotechnica 2010; 5(2): 121-126, https:// doi.org/10.1007/s11440-010-0117-0.
2. Boon C W, Houlsby G T, Utili S. Designing tunnel support in jointed rock masses via the DEM. Rock Mechanics and Rock Engineering 2014; 48(2):603-632, https://doi.org/10.1007/s00603-014-0579-8.
3. Phuor T, Harahap I S H, Ng C Y, Al-Bared M A M. Development of the skew boundary condition for soil-structure interaction in three-dimensional finite element analysis. Computers and Geotechnics 2021; 137: 104264, https://doi.org/10.1016/j.compgeo.2021.104264.
4. Wu N, Liang Z, Zhang Z. Development and verifcation of three-dimensional equivalent discrete fracture network modelling based on the fnite element method. Engineering Geology 2022; 306: 106759, https://doi.org/10.1016/j.enggeo.2022.106759.
5. Feng Q, Xu J S, Cai C X, Liu W W, Jin J C, Han W W, Zhe Q. Damage constitutive model and meso-failure characteristics of freeze-thaw rock triaxial compression. Bulletin of Engineering Geology and the Environment 2024; 83: 122, https://doi.org/10.1007/s10064-024-03594-0.
6. Meng Z S, Ma C, Xie Y Y. Influence of impact load form on dynamic response of chock-shield support. Eksploatacja i Niezawodnosc-Maintenance and Reliability 2023; 25(3): 168316, http://doi.org/10.17531/ein/168316.

7. Chang X K, Wu S C, Cheng H Y, Fu X. Full-waveform Characteristics and Frequency Spectrum of Acoustic Emission for Fine Sandstone, Journal of Yangtze River Scientific Research Institute 2022; 39(07): 118-125, https://doi.org/10.11988/ckyyb.20210249.
8. Do T N, Wu J H. Simulation of the Inclined Jointed Rock Mass Behaviors in a Mountain Tunnel Excavation Using DDA. Computers and Geotechnics 2019; 117: 103249, https://doi.org/10.1016/j.compgeo.2019.103249.
9. Sasong, M, Park, D, Yoo, J, and Li, J S. Experimental and numerical analyses of an opening in a jointed rock mass under biaxial compression. International Journal of Rock Mechanics and Mining Sciences 2011; 48(7): 1055-1067, https://doi.org/10.1016/j.ijrmms.2011.09.001.
10. Yun M C, Ren J X, Zhang L, Zhang K. Research on triaxial compressive mechanical properties and damage constructive model of post-thawing double-fractured quasi-sandstones with different angles. Heliyon 2024; 10: e34268, https://doi.org/10.1016/j.heliyon.2024.e34268.
11. Ren J X, Yun M C, Cao X T L, Zhang K, Liang Y, Chen X. Study on the mechanical properties of saturated red sandstone under freeze-thaw conditions. Environmental Earth Sciences 2022; 81(14): 376, https://doi.org/10.1007/s12665-022-10503-9.
12. Wang Y, Cao Z, Li P, Yi X. On the fracture and energy characteristics of granite containing circular cavity under variable frequency-amplitude fatigue loads. Theoretical and Applied Fracture Mechanics 2023; 125: 103872, https://doi.org/10.1016/j.tafmec.2023.103872.
13. Wen S, Du L, Kong Q, Zhang M, Ding X. Study on Microwave- X assisted TBM Double-edged Cutter Rock-breaking Efficiency and its Positional Relationship, Eksploatacja i Niezawodnosc-Maintenance and Reliability 2024; 26(2): 186447, http://doi.org/10.17531/ein/186447.
14. Mieczkowski G. Criterion for crack initiation from notch located at the interface of bi-material structure. Eksploatacja i Niezawodnosc-Maintenance and Reliability 2019; 21 (2): 301-310, http://dx.doi.org/10.17531/ein.2019.2.15.
15. Cox, S J D, Meredith P G. Microcrack formation and material softening in rock measured by monitoring acoustic emissions. International Journal of Rock Mechanics and Mining Sciences and Geomechanics Abstracts 1993; 30: 11-24, https://doi.org/10.1016/0148-9062(93)90172-A.
16. Kong B, Wang E Y, Li Z H, Wang X R, Liu J, Li N. Fracture mechanical behavior of sandstone subjected to high-temperature treatment and its acoustic emission characteristics under uniaxial compression conditions. Rock Mechanics and Rock Engineering 2016; 49(12): 4911-4918, https://doi.org/10.1007/s00603-016-1011-3.
17. Novikov E A, Oshkin R O, Shkuratnik V L, Epshtien S A, Dobryakova N N. Application of thermally stimulated acoustic emission method to assess the thermal resistance and related properties of coals. International Journal of Mining Science and Technology 2018; 28: 243-249, https://doi.org/10.1016/j.ijmst.2017.12.019.
18. Li X, Li J, He D, Qu Y. Gear pitting fault diagnosis using raw acoustic emission signal based on deep learning. Eksploatacja i Niezawodnosc-Maintenance and Reliability 2019; 21 (3): 403-410, http://dx.doi.org/10.17531/ein.2019.3.6.
19. Li D X, Wang E Y, Kong X G, Ali M, Wang D M. Mechanical behaviors and acoustic emission fractal characteristics of coal specimens with a pre-existing flaw of various inclinations under uniaxial compression. International Journal of Rock Mechanics and Mining Sciences 2019; 116: 38-51, https://doi.org/10.1016/j.ijrmms.2019.03.022.
20. Qiu L M, Song D Z, Li Z H, Liu B B, Liu J. Research on AE and EMR response law of the driving face passing through the fault. Safety Science 2019; 117:184-193, https://doi. org/10.1016/j.ssci.2019.04.021.
21. Liu X X, Wu L X, Zhang Y B, Liang Z Z, Yao X L, Liang P. Frequency properties of acoustic emissions from the dry and saturated rock. Environmental Earth Sciences 2019; 78(3): 67, https://doi.org/10.1007/s12665-019-8058-x.
22. Martin C D, Chandler N A. The progressive fracture of Lac du Bonnet granite. International Journal of Rock Mechanics and Mining Sciences and Geomechanics Abstracts 1994; 31(6): 643-659, https://doi.org/10.1016/0148-9062(94)90005-1.
23. Mark S D. Mechanistic interpretation and practical application of damage and spalling prediction criteria for deep tunneling. Canadian Geotechnical Journal 2007; 44(9): 1082-1116, https://doi.org/10.1139/T07-033.
24. Zhao X G, Cai M, Wang J, Ma L K. Damage stress and acoustic emission characteristics of the Beishan granite. International journal of Rock Mechanics and Mining Science 2013; 64(12): 258-269, https://doi.org/10.1016/j.ijrmms.2013.09.003.
25. Zhu J，Deng J H, Huang Y M, Yu Z Q. Experimental study on the characteristic strength of saturated marble. Chinese Journal of Rock Mechanics and Engineering 2019; 38(06): 1129-1138, https://doi.org/10.13722/j.cnki.jrme.2018.1302